Materials Advances

ROYAL SOCIETY OF CHEMISTRY

PAPER

View Article Online
View Journal | View Issue

Cite this: *Mater. Adv.*, 2022, 3, 1737

Solution-based low-temperature $CsPbI_3$ nanoparticle perovskite solar cells†

Adva Dayan Shpatz, ‡[a] Stav Rahmany, ‡[a] Flatken Marion, [b] Tal Binyamin,[a] Armin Hoell, [b] Antonio Abate[b] and Lioz Etgar *[a]

Received 2nd September 2021,
Accepted 19th December 2021

DOI: 10.1039/d1ma00802a

rsc.li/materials-advances

This work reports on low-temperature inorganic $CsPbI_3$ perovskite nanostructures synthesized as the active black phase, without the additional use of organic ligands and based only on CsI and PbI_2 precursors. This new method is based on the "inverse temperature crystallization" (ITC) phenomenon where dissolved lead salts tend to form nucleation grains at high temperatures. This methodology allows the conversion temperature of the $CsPbI_3$ black phase to be reduced without the use of additives or anti-solvent treatment. We use small angle X-ray scattering (SAXS), high-angle annular dark-field scanning transmission electron microscopy (HAADF-STEM), and photoluminescence (PL) measurements to characterize the precursor solutions at different heating times to understand the nature of the observed $CsPbI_3$ nanoparticles (NPs). Heating the solution for 192 hours shows the high-quality black active phase of $CsPbI_3$ NPs after evaporation of the solvent in the solid state. This allows us to form a film of $CsPbI_3$ in its photoactive phase at a low temperature (T = 55 °C) within a few minutes using no additives or antisolvent treatment. We use the dispersion of $CsPbI_3$ nanostructures to fabricate black-phase $CsPbI_3$ perovskite-based solar cells on a mesoporous TiO_2 structure showing a power conversion efficiency of 7.3%.

Introduction

Perovskite solar cells (PSCs) have been significantly improved in recent years, where state-of-the-art PSCs demonstrate a power conversion efficiency (PCE) of more than 25.5%.[1] In spite of the unique properties of perovskites, such as a tunable bandgap, a long electron–hole diffusion length, and a low-cost fabrication process, their thermal stability is still an unsolved problem.[2,3] Perovskites have an ABX_3 structure where A is a monovalent organic or inorganic cation (*e.g.*, MA^+ = methylammonium, FA^+ = formamidinium, Cs^+ or Rb^+), B is a divalent metal cation (Pb^{2+} or Sn^{2+}) and X is a halide anion (I^-, Br^- or Cl^-). Today, state-of-the-art perovskites used for PSCs are composed of organic A site cations (MA^+, FA^+, or a combination of both).[4,5] Recent studies have shown that the incorporation of an inorganic cation into the perovskite structure can increase the thermal stability of the material.[6,7] Cs^+ is an excellent candidate to replace the organic cation in the perovskite lattice in terms of enhancing the thermal stability.[8,9] However, it suffers from instability upon exposure to air.[10] In the case of $CsPbI_3$, four different temperature-dependent polymorphs have been reported: α (cubic), β (tetragonal), γ (orthorhombic), and δ (also orthorhombic), of which only the first three are photovoltaic (PV) active. Polymorphs α, β and γ are related to the active phases that demonstrate a black color, while δ represents the non-active yellow phase.[11]

The formation of Cs-based perovskite active phases (α, β and γ) without any additives requires a high annealing temperature (~350 °C), which complicates the fabrication process. In addition, Cs-based perovskites are unstable under standard ambient conditions due to moisture sensitivity, leading to conversion of the PV-active phases (α, β, and γ) to the yellow, non-active phase (δ) in just a few minutes.

In order to reduce the ΔH_f^0 (formation temperature) of the $CsPbI_3$ active phase, one possibility is to use additives. Snaith *et al.* used hydriodic acid (HI) as an additive to reduce the annealing temperature to 100 °C.[12] Furthermore, the addition of HI affects the grain size of the perovskite thin film and results in the formation of a more uniform layer. Using a similar approach, $PbI_2{\cdot}x$HI and CsI precursors have been used to reduce the conversion temperature to 150 °C, obtaining a PCE of 7.6% for the full device.[13] Another way to overcome the high conversion temperature is to include different salts, such as CaI_2, $EuBr_2$ and $EuCl_3$, which reduces the total formation energy by increasing the entropy of the system, therefore

[a] *Institute of Chemistry, Casali Center for Applied Chemistry, The Hebrew University of Jerusalem, Jerusalem 91904, Israel. E-mail: lioz.etgar@mail.huji.ac.il*
[b] *Helmholtz-Zentrum Berlin für Materialien und Energie GmbH, Hahn-Meitner-Platz 1, 14109 Berlin, Germany*

† Electronic supplementary information (ESI) available. See DOI: 10.1039/d1ma00802a

‡ Equal contribution.

lowering the annealing temperature drastically.[14–16] In addition, the incorporation of barrier molecules to form a two-dimensional (2D) structure helps to stabilize the $CsPbI_3$ active phase.[13,17] In this regard, different molecules have been studied: linear molecules, aromatics, diamines and others. As a result, the perovskite structure becomes more stable and the conversion temperature is reduced to ~100–150 °C.[13,17–20] Liu *et al.* demonstrated an efficient $CsPbI_3$ quantum dot (QD)-based solar cell with improved conductivity and stability for both temperature and humidity *via* the incorporation of μ-graphene.[21] Further improvement in QD-based devices has been achieved using $CsPbI_3$ and $CsPbI_{2+x}Br_{1-x}$ with tunable bandgaps.[22] Even though different additives can reduce the annealing temperature, in most cases these additives are still present in the perovskite film after its formation, which can harm the PV performance. Here we report on a new method to reduce the conversion temperature of the $CsPbI_3$ black phase without using any additives or anti-solvent treatment. Importantly, the addition of salts to the $CsPbI_3$ perovskite solution will create a change in the bonding angles of the lattice due to the size difference of the A site cation, which can result in lower symmetry. Moreover, the addition of HI will add undesirable H_2O molecules to the precursor solution.[12,23,24] The incorporation of barrier molecules as additives will form organic–inorganic hybrids rather than fully inorganic perovskites.[13,25] Finally, the use of antisolvents is restricted to the fabrication of small cells and requires a lot of the parameters to be controlled.[26] Our method is based on the "inverse temperature crystallization" (ITC) phenomenon in which dissolved lead salts tend to form nucleation grains at high temperatures, as presented by Bark *et al.*[27] Due to the predominant contrast differences in the specimen, in this work we refer to the liquid precursor as a dispersion rather than a solution in the strict sense. Based on ITC we enable the formation of a dispersion that contains the black phase of $CsPbI_3$ nanoparticles (NPs) and nano-rods (NRs) (without the involvement of organic ligands) using only CsI and PbI_2 precursors. Unlike conventional $CsPbI_3$ NPs/NRs, the lack of organic ligands in our solution allows the formation of perovskite films without any organic residues that can damage the charge transport within the layer, which results in a high current density.[28] Deposition of this perovskite dispersion allows us to achieve the desirable black $CsPbI_3$, PV-active phase at a low temperature (T = 55 °C) within a few minutes. Due to this simple formation process, we were able to fabricate $CsPbI_3$ PSCs on a mesoporous TiO_2 structure for the first time. The solar cell demonstrates a current density (J_{sc}) of 20.2 mA cm^{-2}, which results in a PCE of 7.3%.

Results and discussion

Fig. 1 presents the different available routes to reduce the conversion temperature of $CsPbI_3$.[12,29,30] Most of the methods are based on including additives, while the method reported in this work (in the blue frame) is based on the preceding formation of $CsPbI_3$ NRs and NPs in the solution. The corresponding $CsPbI_3$ dispersion is prepared by dissolving CsI and PbI_2 in DMSO. Following complete dissolution of the precursors, the "fresh" solution is heated using an oil bath at 180 °C for more than 48 hours. In the course of this process, the color of the solution changes from light yellow to dark brown-black, which indicates the chemical and physical changes in the solution. This phenomenon is known as ITC,[27,31] where lead nucleation grains are formed as a result of increasing temperature, serving as nucleation seeds for the growth of the $CsPbI_3$ nanorods and nanoparticles.[27,32] Nowadays, ITC is used to form perovskite single crystals that tend to dissolve when left in the solvent for

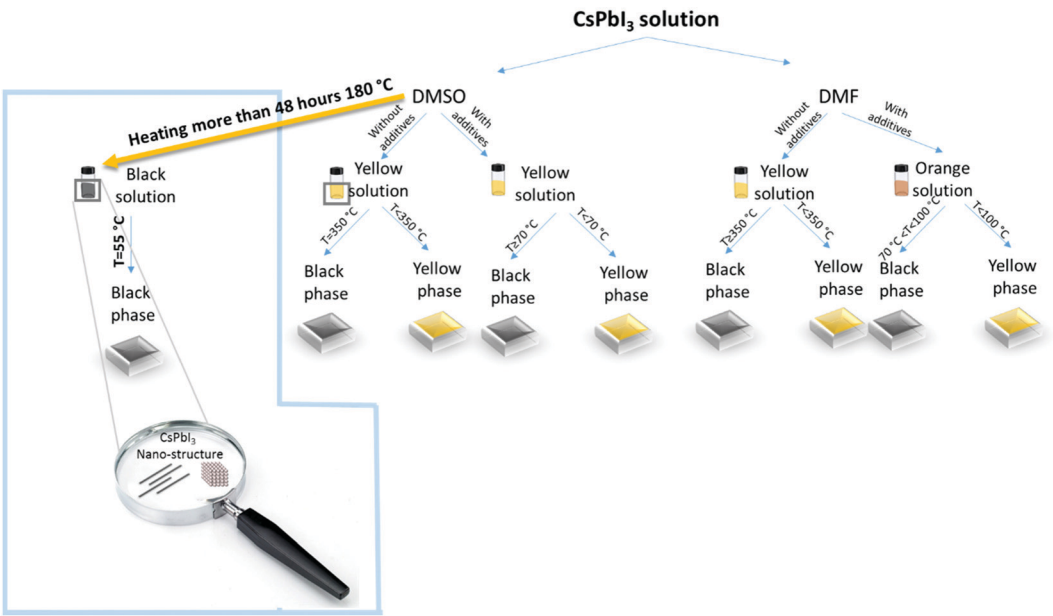

Fig. 1 Schematic illustration of common cesium-based perovskite solutions and the different conversion temperatures.[12,14,15,17] The blue frame shows the process of $CsPbI_3$ nano-rod and NP formation reported in this work.

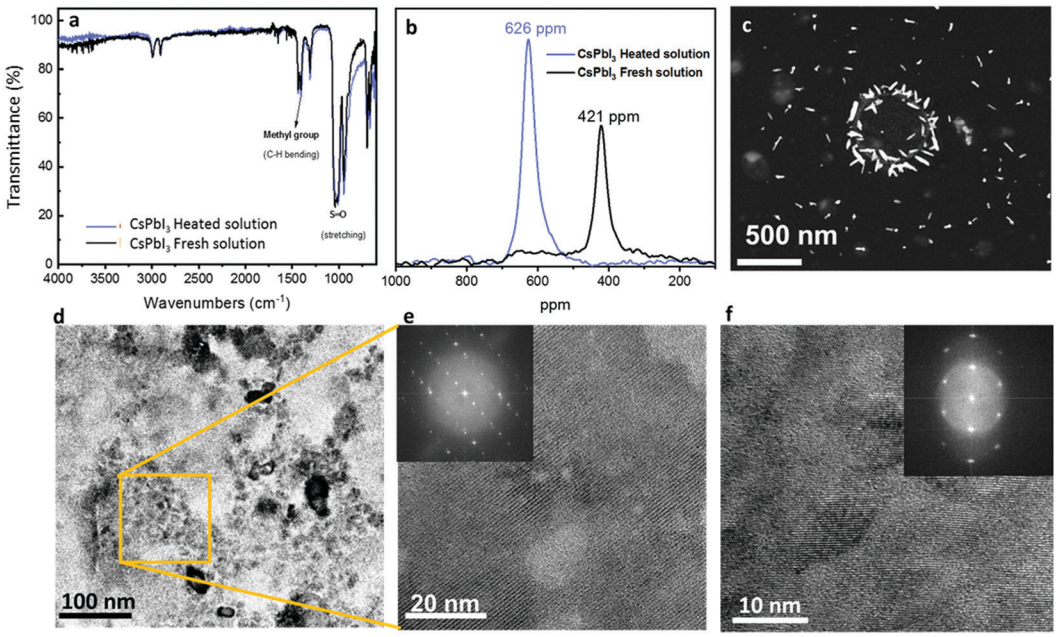

Fig. 2 (a) Fourier transform infrared (FTIR) spectra of the $CsPbI_3$ solution before (black) and after (light blue) heating to 180 °C for 72 h. (b) ^{207}Pb NMR spectra of the $CsPbI_3$ solution before (black) and after (light blue) heating to 180 °C for 72 h. (c) Scanning transmission electron microscopy (STEM) and (d) transmission electron microscopy (TEM) images of the $CsPbI_3$ NPs from the $CsPbI_3$ dispersion after heat treatment (after solvent evaporation under vacuum). (e) and (f) Enlargement of the $CsPbI_3$ particles where the insets show the diffraction patterns from which the *hkl* crystallographic planes were calculated.

a long time. In this work, we noticed that the solution maintains its brown color for weeks without any visible change, which indicates a stable system. The first verification of the presence of NPs in the solution was the observation of the Tyndall effect. According to the Tyndall effect in colloidal solutions, there will be light scattering by the particles inside the solution, which will enable the beam path to be seen through the solution itself.[33] Fig. S1 (ESI†) presents the Tyndall effect where a laser beam can go through freshly prepared and heated $CsPbI_3$ solutions. In order to understand the content of the solution we performed Fourier transform infrared (FTIR) spectroscopy under several conditions as shown in Fig. 2a. This measurement is used for characterization of the chemical compounds according to their absorption spectra in the infrared region (750 nm to 1 mm). A molecule that absorbs light in this range starts to vibrate and to oscillate around a constant equilibrium point. The absorbed wavelengths correspond to the unique vibrational modes that exist in the molecule, while the rest of the light passes without being absorbed. The shape of the resulting FTIR spectrum constitutes a fingerprint of the material and allows its unambiguous identification. It has been reported that a complex of PbI_2–DMSO can be formed *via* the intermediate phase.[34] The marked vibrations (stretching/bending) are related to the solvent (DMSO) S=O and CH_3 groups. Moreover, it can be seen that both samples show the same pattern, which indicates that the PbI_2–DMSO complex is not present after the heating process. In order to confirm that there are no other DMSO complexes forming with the two salts (CsI and PbI_2), FTIR measurements for DMSO only, PbI_2 in DMSO, and CsI in DMSO without heating and after 72 hours of heating are shown in Fig. S2a–S2c (ESI†), respectively. All three cases show no additional peaks besides the peaks that are related to DMSO. In addition, ^{1}H-NMR measurements (Fig. S5, ESI†) of the $CsPbI_3$ film at different annealing temperatures show that there is no remaining DMSO in the perovskite $CsPbI_3$ film after the annealing process.

To eliminate any cesium-based complex formation after the heating process we performed ^{133}Cs-NMR measurements, as shown in Fig. S3 (ESI†). We found a negligible shift (0.9 ppm) between the fresh and heated solutions. Based on the Cs-NMR and FTIR results, it can be concluded that there is no change in the chemical environment of Cs. However, the recorded ^{207}Pb NMR spectrum shows that the chemical environment of lead is changing based on the temperature of treatment. As presented in Fig. 2b, the peak for the fresh solution appears at 626 ppm, whereas the peak of the heat-treated dispersion appears at a lower value, at 421 ppm. Consequently, heat treatment of the initial precursor solution results in higher shielding of the lead core in the solution, which causes a shift to lower ppm values. This can be interpreted to mean that the initial complexation of Pb(II) is altered by the temperature treatment, creating a modified chemical environment with a stronger effect of electron density shielding the Pb(II) nucleus.[35]

To reveal the nature of the color change as a result of the heating process we took a closer look at the aged solution using scanning electron transmission microscopy (STEM), as can be seen in Fig. 2c. Interestingly, We observed mainly NPs with an average length of ~70 nm. The NPs are organized on the sample's substrate as a ring structure due to the evaporation of the solvent. High-resolution transmission electron microscopy (TEM) images of the $CsPbI_3$ NPs can be seen in Fig. 2d,

where the NPs formed clusters. Higher magnification of these clusters (Fig. 2e and f) reveals clear crystallographic planes on which fast Fourier transform (FFT) was performed (insets of Fig. 2e and f). The diffraction patterns of the NRs are related to the crystallographic planes: (320), (200) and (220), which are related to the α phase of $CsPbI_3$, and where the favorable crystallographic plane is (200), which is a result of the growth conditions.

By using STEM it is possible to identify the particles either *via* electron diffraction or elemental analysis using EDS (energy dispersive X-ray spectroscopy). EDS is based on measuring the characteristic X-ray fluorescence emitted due to the interactions of high-velocity electrons with the sample atoms. Each atom has a different signal due to the difference in the energies of the atoms' shells. Fig. 3 shows EDS and STEM images of the $CsPbI_3$ NPs. Two different kinds of NPs can be recognized: Fig. 3a–d show small NPs and Fig. 3e–h show larger NPs. In the case of the larger NPs (Fig. 3e–h) we successfully performed FFT analysis that confirms the orthorhombic phase. Fig. S6 (ESI†) shows the STEM image of this diffraction. However, we were not able to perform electron diffraction in the case of the small NPs due to the instability of the NPs under the electron beam. For further characterization of the NPs we performed small angle X-ray scattering (SAXS) using synchrotron radiation.[35] The resulting scattering curves are given in Fig. 3i and j. To obtain further information about the dimensions of the present particles and the interactions in the samples, the SAXS curves were fitted using the SASfit© program. This software provides several combinations of form and structure factor models to describe the measured scattering curves. In either case (i) untreated and (j) temperature treated two dimensions can be observed. Small particles with a pronounced interaction are dominant in both states (spherical form factor with a radius r = 0.3 nm). In addition, the SAXS curves indicate the presence of larger particle sizes with a spherical form factor with a dimension of $r \approx 0.9$ nm. Comparing the heat-treated sample with the

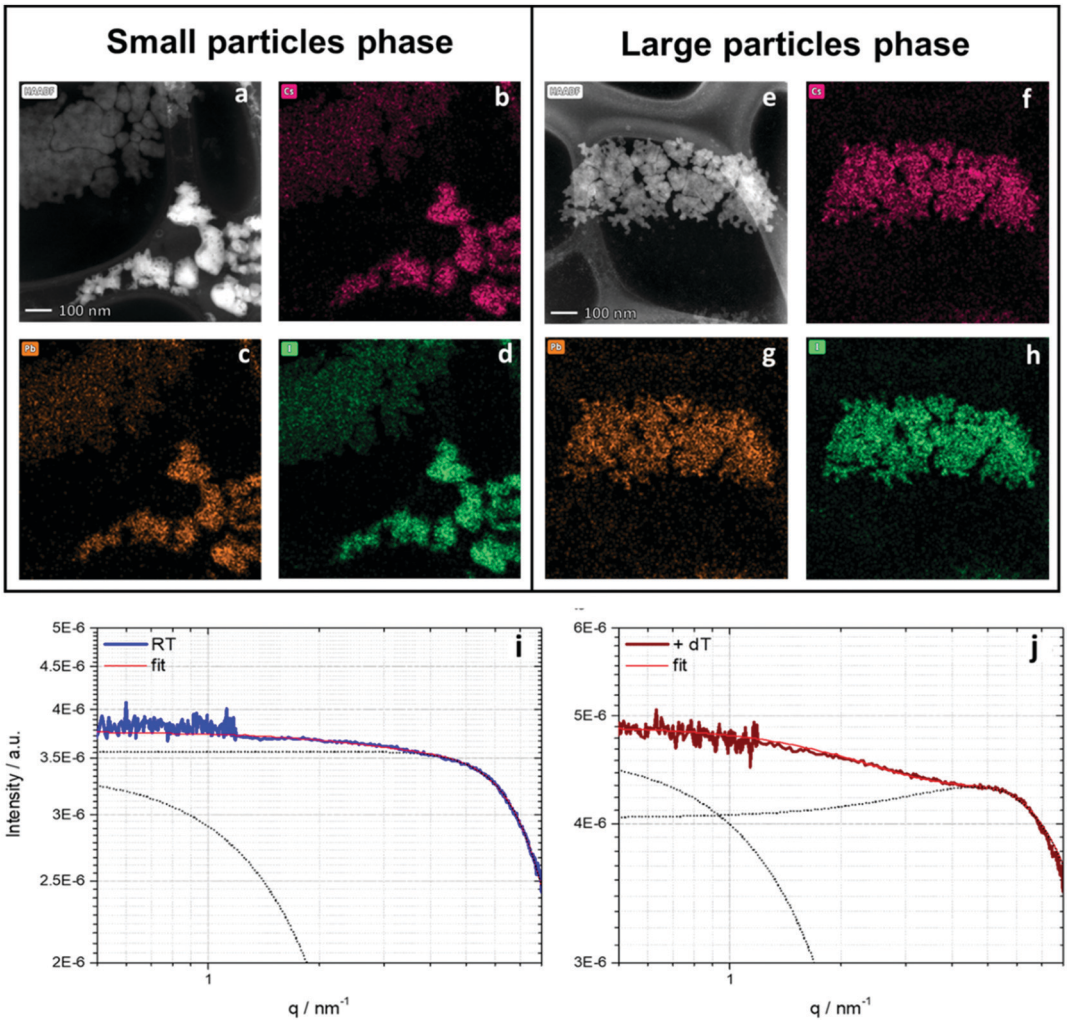

Fig. 3 (a) HAADF STEM image of small particles phase $CsPbI_3$. EDS maps of (b) cesium, (c) lead and (d) iodine. (e) HAADF STEM image of large (orthorhombic) phase $CsPbI_3$. EDS maps of (f) cesium, (g) lead and (h) iodine. (i) and (j) SAXS curves of the perovskite precursor solution in DMSO: scattering curve of the (i) fresh solution (RT, blue); and (j) solution heat-treated for 72 hours (dT, brown) at a concentration of 0.8 mol L^{-1}. In both curves, the thin red line represents the model fit, and the black dashed lines depict the respective contributions.

untreated sample, the specific interaction of particles is more pronounced in the case of the heat-treated sample. This is displayed by a stronger expression of the structure factor maximum at higher q-values, providing an inter-particle distance of roughly 1.2 nm. This evolution can be interpreted as a first indication of a pre-crystalline arrangement in the precursor solution, which gives rise to an expected faster crystallization process triggered by the thermal treatment.

An additional interesting observation was the color change of the $CsPbI_3$ solution with temperature. The $CsPbI_3$ solution gets darker upon continuous heating (as can be seen in Fig. 4d). In order to understand the effect of the heating time on the particle solution we performed photoluminescence (PL) measurements for the $CsPbI_3$ solution after 48 h, 144 h, and 192 h of heating at 180 °C, as presented in Fig. 4a–c, respectively. Each solution was excited at several wavelengths (from 480 nm to 620 nm in 20 nm increments). All cases show the same trend: the PL peak is red-shifted as the excitation wavelength becomes longer. This behavior leads to the assumption that the heated solution contains several populations of particles including the active (α and β) and inactive (δ) $CsPbI_3$ phases in different sizes that range between ~5 nm and 15 nm.[36] In addition, it can be observed that a long heating time also creates a red shift at each excitation wavelength. It can be seen that in the case when the solutions are excited at 480 nm the peak shifts from 558 nm for 48 h of heating to 590 nm and 627 nm for 144 h and 192 h of heating, respectively. The same trend is observed at each excitation wavelength. This shift is an indication that in the case of the long heating time the formation of the active phase is preferable, which creates particles emitting at long wavelengths.

Furthermore, we observed that the range of the excitation wavelength (*i.e.*, 480–620 nm) becomes shorter upon continuous heating, decreasing from 105 nm to 83 nm, and 78 nm for 48 h, 144 h, and 192 h, respectively. This decrease indicates a narrow size distribution of the $CsPbI_3$ particles and better conversion of the active phase upon continuous heating of the solution. To support this claim, we extracted the full width at half maximum (FWHM) of the PL peaks for all three solutions (48 h, black squares; 144 h, red circles; and 192 h, blue triangles) presented in Fig. 4e. The graph presents two regions, from 550 nm to 610 nm (yellow), which refers to the non-active phase of $CsPbI_3$, and from 610 nm to 720 nm (brown), which is the characteristic region of the active phase.[36,37] Each point represents the PL peak position at a specific excitation wavelength. The PL peak position is red-shifted while the FWHM becomes narrower for all three heating times. The narrow FWHM for the longer heating time suggests an efficient conversion of the inactive phase of $CsPbI_3$ to an active phase and thus results in a smaller particle size distribution.

Another trend depicted in Fig. 4e is that upon prolonged heating the PL peak position is shifted towards the active-phase region. In the case of the shortest heating time (48 h) it can be seen that the PL peak position is located within the active-phase region only when excited using a wavelength of 610 nm (the 5th point in the graph) or higher. When heated for 192 h, all PL peak positions are located in the active-phase region. This is a clear indication that a long heating time of the solution is essential to form a dispersion of active-phase $CsPbI_3$ NPs from the original precursor solution. Moreover, we study the film formation of $CsPbI_3$ from regular (untreated) and

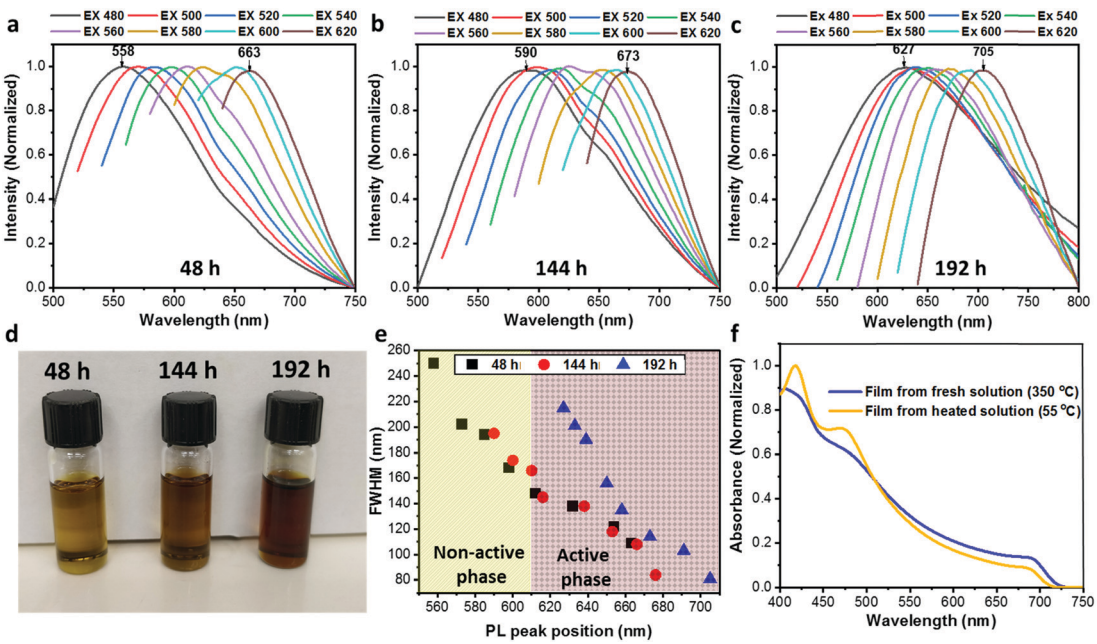

Fig. 4 Photoluminescence (PL) measurements for $CsPbI_3$ solutions after (a) 48 h, (b) 144 h and (c) 192 h of heating (180 °C) using different excitation wavelengths. (d) Images of the $CsPbI_3$ solution after different heating times. (e) FWHM as a function of the PL peak position for the solution after heating for 48 h (black), 144 h (red), and 192 h (blue). (f) Absorbance spectra of the $CsPbI_3$ film made from a standard solution (blue) and a solution heated for 144 h (orange).

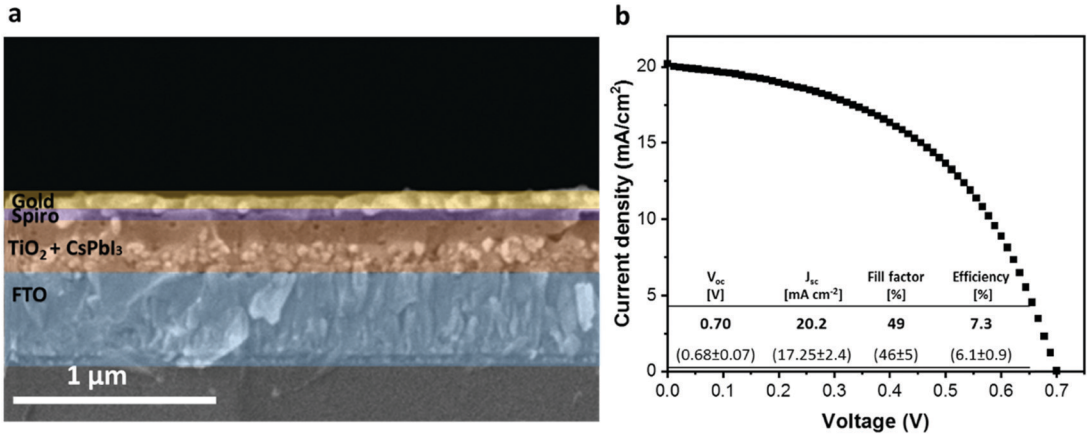

Fig. 5 (a) SEM cross-section of the full device fabricated from the heated $CsPbI_3$ solution. (b) *J*–*V* curve of the best device. The table shows the PV parameters of the best device (bold) and the average of 25 devices (in brackets), which are from a solution that was heated for 72 hours.

heated solutions. The regular film was annealed at 350 °C to achieve the black active phase, while the film formation from the heated solution occurred already at 55 °C, changing color from yellow to the black, PV-active phase. Fig. 4f shows absorbance spectra for $CsPbI_3$ films that were made using a fresh solution (blue) and using a solution heated for 72 hours (yellow). The first was annealed at 350 °C with an anti-solvent treatment to achieve the active phases, while the heated solution was annealed at 55 °C converting to the active phase without any anti-solvent treatment. Both films have the same general absorbance shape, while the onset of the heated solution (yellow) is slightly blue-shifted, probably due to some residues belonging to a residual PV non-active phase. The film that was made using the heated solution presented a brownish-black color, as can be seen in Fig. S4 (ESI†).

Subsequent to the solution characterizations we used the dispersion of active-phase $CsPbI_3$ NPs for solar cell fabrication using a mesoporous TiO_2 substrate as the photo anode on which the dispersion of NPs was spin-coated before annealing. The common annealing temperature of the active $CsPbI_3$ (α, β, and γ) phases is 350 °C.[18] By contrast, the conversion of the $CsPbI_3$ dispersion to the black phase on mesoporous TiO_2 occurs within a few seconds at a low temperature of 55 °C without requiring any anti-solvent treatment during the perovskite-deposition process. It can be assumed that the NPs serve as nucleation sites for the crystal growth of the perovskite and thus reduce the energy required for the formation of the active phase. Since the annealing temperature in our case is significantly lower than the boiling point of DMSO (189 °C)[38] we assume that residual solvent molecules may remain in the formed perovskite film. However, choosing a higher annealing temperature (>100 °C) meant that the perovskite film degraded after several minutes of annealing, changing its color from black-brown to yellow. By contrast, at 55 °C the film can be annealed for more than 30 min without any color change. To ensure that the solvent evaporated completely we kept the annealed perovskite film in a nitrogen environment for 24 h. A cross-section of the full solar cell can be seen in Fig. 5a. The corresponding perovskite layer was prepared using the $CsPbI_3$ NP dispersion on a ∼110 nm mesoporous TiO_2 layer. The perovskite forms a thin and uniform layer of ∼200 nm. As can be seen, the $CsPbI_3$ NPs form a continuous layer along the entire TiO_2 region, which contributes to efficient charge transfer. The good penetration of the $CsPbI_3$ NPs into the porous layer is possible due to the smaller size of the NPs (∼5–15 nm) compared with the pore size of the TiO_2. The formation of the $CsPbI_3$ active phase on top of mesoporous TiO_2 was not achieved before, and we attribute this to the presence of PV-active $CsPbI_3$ NPs in the solution, which function as nucleation sites for the formation of the black phase of $CsPbI_3$ on top of the mesoporous TiO_2.

$$\mathrm{HI} = \frac{J_{\mathrm{rev}}\left(\frac{V_{\mathrm{OC}}}{2}\right) - J_{\mathrm{for}}\left(\frac{V_{\mathrm{OC}}}{2}\right)}{J_{\mathrm{rev}}\left(\frac{V_{\mathrm{OC}}}{2}\right)}$$

The champion device based on the $CsPbI_3$ NPs demonstrates a J_{sc} value of 20.2 mA cm^{-2}, which results in a PCE of 7.3%. This is the first demonstration of low-temperature $CsPbI_3$ crystallization without additives deposited on the mesoporous TiO_2 structure. Our champion cell shows a high efficiency compared with other devices based on $CsPbI_3$ without any additives (yellow region), as shown in Fig. S7 (ESI†). In the other region (green in Fig. S7, ESI†) there are devices in which additives were used in order to form the active phase, where most of them are fabricated with an inverted architecture.

We found that the HI (hysteresis index), calculated as described in eqn (1) for these kinds of cells is ∼0.14, where $J_{\mathrm{rev}}\left(\frac{V_{\mathrm{OC}}}{2}\right)$ and $J_{\mathrm{for}}\left(\frac{V_{\mathrm{OC}}}{2}\right)$ are the values of each J_{sc} at half of the V_{oc} value (Fig. S8, ESI†).

Conclusions

This work presents the low-temperature dispersion of inorganic $CsPbI_3$ perovskite NPs, synthesized as the active black phase

through continuous heating for 192 hours without any additional use of organic ligands and based only on CsI and PbI_2 precursors. As a result, it was possible to form a thin film of the $CsPbI_3$ active phase at a low temperature (55 °C) without the use of any additive or anti-solvent treatment. Using the $CsPbI_3$ NP dispersion we were able to form for the first time a $CsPbI_3$ perovskite layer on mesoporous TiO_2 in a solar cell. The solar cell demonstrates a current density (J_{sc}) of 20.2 mA cm^{-2}, which results in a PCE of 7.3%. Using SAXS, FTIR and STEM analyses we were able to reveal the nature of this $CsPbI_3$ perovskite NP dispersion. The $CsPbI_3$ NPs function as nucleation sites in the dispersion for the formation of the black phase of $CsPbI_3$ on top of mesoporous TiO_2, which enables the formation of the PV-active phase at low temperatures without additives. This work demonstrates the low-temperature solution-processed black phase of $CsPbI_3$, which can function as a light harvester in the solar cell.

Experimental

Device fabrication

SnO_2/(FTO) conductive glass (10 ohm cm^{-1}, Pilkington) was etched *via* the reaction of zinc powder with HCl (37% Sigma) on top of the glass. After etching, the glass was cleaned using a sonication bath for 15 minutes followed by oxygen plasma treatment (80% power, Diener). The compact TiO_2 layer (TiDIP, 75% in isopropanol, Aldrich, diluted 1 : 5 in isopropanol) was deposited on the substrate by spin coating (5000 rpm for 30 seconds) and annealed for 450 °C for 30 minutes. This was followed by the deposition of m-TiO_2 nanoparticles (30-NRD, dyesol) (1 : 8 w/w% in ethanol absolute) by spin-coating (5000 rpm for 30 seconds), where the annealing was at 325 °C for 10 minutes, 450 °C for 10 minutes, and 500 °C for 30 minutes.

For the perovskite deposition, 85 ml of perovskite solution was added dropwise onto the middle of the substrate, followed by a spin-coating process with a five second delay time, a ten second spin at 1000 rpm, and a 45 second spin at 2000/3500/5000 rpm. The cells were annealed at 55 °C for 30 minutes. Then, 40 μL of 0.06 M 2,2′,7,7′-tetrakis-(*N*,*N*-di-4-methoxyphenylamino)-9,9′-spirofluorine (spiro-OMeTAD) in chlorobenzene with additives of 26.2 μL/1 mL bis(trifluoromethane) sulfonimide lithium salt in acetonitrile (520 mg mL^{-1}), 29.0 μL/1 mL tris(2-(1H-pyrazol-1-yl)-4-*tert*-butylpyridine)-cobalt(III) tris(bis(trifluoromethylsulfonyl)imide)) in acetonitrile (300 mg mL^{-1}) and 19.2 μL/1 mL of 4-*tert*-butylpyridine (Aldrich) was spin coated at 4000 rpm for 30 s. Finally, a 70 nm-thick gold electrode was thermally evaporated on the film under a vacuum of $\sim 10^{-7}$ Torr.

Preparation of perovskite solutions

The perovskite solutions were prepared using a nitrogen-filled glovebox. All of the inorganic precursors were purchased from Sigma Aldrich. A $CsPbI_3$ solution of 1 M was prepared by dissolving CsI and PbI_2 in dimethyl sulfoxide (DMSO). The perovskite solutions were prepared 12 hours before being placed in an oil bath. After 12 hours the solution was transferred to an oil bath at 180 °C for 72 hours.

Encapsulation

Encapsulation was done using a Meltonix 1170-60 (Solaronix) instrument and cover glasses (PAUL MARIENFELD) under a nitrogen environment.

Absorbance measurements

Absorbance measurements were performed using a Jasco V-670 spectrophotometer.

Ultra-high-resolution scanning electron microscopy (UHR-SEM)

The images were obtained by using a Magellan XHRSEM system of FEI (Field Emission Instruments), The Netherlands. The measurement conditions were 10 kV.

Photovoltaic characterization

Photovoltaic measurements were performed using a Newport system, composed of an Oriel *I–V* test station using an Oriel Sol3A simulator. The solar simulator is class AAA for spectral performance, uniformity of irradiance, and temporal stability. The solar simulator is equipped with a 450 W xenon lamp. The output power is adjusted to match AM1. The spectrally matched classic cations are IEC60904-9 2007, JIC C 8912, and ASTM E927-05.

Fourier transform infrared spectroscopy (FTIR)

The Fourier transform infrared spectroscopy (FTIR) data were collected using an FTIR PerkinElmer Spectrophotometer (Spectrum 400 FT-IR). All the samples were pre-frozen using liquid nitrogen and freeze dried at −50 °C in a vacuum chamber. 0.01 gram of each sample was milled and mixed with 0.3 g of KBr powder, then pressed into appropriate tablets. All the data were collected in transmittance mode.

High-resolution transmission electron microscopy (HRTEM)

The morphology and elemental composition of the NPs were analysed using HR (S)TEM (high-resolution scanning transmission electron microscopy), a Tecnai F20 G2 (FEI Company, USA) system. Sample preparation was performed as follows: 3.5 μL of the NC dispersion was added dropwise onto a copper grid coated with an amorphous carbon film, and then the solvent was evaporated using a vacuum chamber. Elemental analysis of the NCs was performed using EDAX EDS (energy dispersive X-ray spectroscopy) where the microscope was operated in STEM mode at an accelerating voltage of 200 kV.

^{133}Cs-NMR

The ^{133}Cs-NMR spectra were acquired using a Bruker 500 MHz Avance II NMR spectrometer with a ^{133}Cs reference frequency of 65.607 MHz. Sixteen scans were acquired using a 90° pulse and a 2.8 s repetition time.

^{207}Pb-NMR

The ^{207}Pb-NMR spectra were acquired using a Bruker 500 MHz Avance II spectrometer. The solvent was DMSO. NS: 4096, DS:0,

SWH: 1071420.625 Hz, FIDEWS: 65.394817 Hz, AQ: 0.0152917 sec.

^{1}H-NMR

The ^{1}H-NMR spectra were acquired using a Bruker 500 MHz spectrometer. The solvent was DMSO. NS: 16, DS:2, SWH: 10416.67 Hz, FIDEWS: 0.635783 Hz, AQ: 1.5728641 sec.

The ^{133}Cs-NMR spectra were acquired using a Bruker 500 MHz Avance II NMR spectrometer with a ^{133}Cs reference frequency of 65.607 MHz. Sixteen scans were acquired using a 90° pulse and a 2.8 s repetition time.

Small angle X-ray scattering (SAXS)

The SAXS measurements were performed using synchrotron radiation at the four crystal monochromator beamline in the laboratory of PTB (Physikalisch-Technische Bundesanstalt) at BESSYII.[39] The SAXS instrument of Helmholtz-Zentrum Berlin (HZB) contains an adjustable, about 3 m long, support structure with a long edge-welded bellows system to enable the changing of the sample-to-detector distance.[40] The 2D scattering images were collected using a windowless Dectris 1M PILATUS2 in-vacuum hybrid-pixel detector. The measurements were carried out at two different distances (0.8 m and 3.7 m) at photon energies of 10 keV and 8 keV, respectively. Thus, a q-range from 0.05 nm^{-1} to 8.5 nm^{-1} was covered (size range of 125.6 nm to 0.74 nm in real space). The precursor solutions were measured using an acquisition time of 600 s with three repetitions for the short distance and long distance to achieve good-quality data and to monitor unwanted but possible changes of the specimen over time (which can therefore be safely excluded). Due to the low transmittance of the lead-containing precursor solutions, especially thin (0.1 mm) rectangular borosilicate cuvettes (purchased from CM Scientific, UK) were used.

Data reduction, radial averaging and fitting: for data reduction and for radial averaging of the 1D scattering pattern the BerSAS software was used, an advanced version of the BerSANS software[41] that is applicable for SAXS and SANS. All SAXS curves of the investigated samples were fitted using the program SASfit.[42] In order to get a general idea of the order of magnitude a structure model that includes a spherical form factor and a hard-sphere structure factor was chosen to fit all sample scattering curves. The herein investigated particles were considered as hard spheres. Thereby, these particles are assumed to be incompressible, resulting in a fixed radius for each particle and an infinite repulsive force at a certain interparticle separation. The hard-spheres model neglects attractive forces but describes fairly well a various number of colloids in organic solvents.[43–45] We used the Percus–Yevick approximation for hard spheres to fit the interaction of the analyzed particles.[46,47]

Conflicts of interest

There are no conflicts to declare.

Acknowledgements

This work was supported by the Israel Science Foundation grant number 937/18 and by the Israel Ministry of Energy. This work was done under the Hybrid Integrated Systems for Conversion of Solar Energy (HI-SCORE) graduate research school between Helmholtz-Zentrum Berlin für Materialien und Energie (HZB) and the Hebrew University of Jerusalem.

References

1 Best Research-Cell Efficiency Chart, NREL Photovoltaic Research, 2021 https://www.nrel.gov/pv/assets/pdfs/best-research-cell-efficiencies.20191106.pdf (accessed May 30, 2021).
2 M. R. Filip, G. E. Eperon, H. J. Snaith and F. Giustino, Steric Engineering of Metal-Halide Perovskites with Tunable Optical Band Gaps, *Nat. Commun.*, 2014, **5**, 1.
3 Y. Lv, Y. Guo, H. Zhang, X. Zhou and H. Chen, Enhanced Efficiency and Stability of Fully Air-Processed TiO_2 Nanorods Array Based Perovskite Solar Cell Using Commercial Available CuSCN and Carbon, *Sol. Energy*, 2018, **173**, 7–16.
4 R. J. Sutton, G. E. Eperon, L. Miranda, E. S. Parrott, B. A. Kamino, J. B. Patel, M. T. Hörantner, M. B. Johnston, A. A. Haghighirad and D. T. Moore, *et al.*, Bandgap-Tunable Cesium Lead Halide Perovskites with High Thermal Stability for Efficient Solar Cells, *Adv. Energy Mater.*, 2016, **6**(8), 1502458.
5 A. S. Dayan, X. Zhong, M. Wierzbowska, C. E. M. Oliveira, A. Kahn and L. Etgar, The Properties, Photovoltaic Performance and Stability of Visible to Near-IR All Inorganic Perovskite, *Mater. Adv.*, 2020, **1**, 1920–1929.
6 J. K. Nam, S. U. Chai, W. Cha, Y. J. Choi, W. Kim, M. S. Jung, J. Kwon, D. Kim and J. H. Park, Potassium Incorporation for Enhanced Performance and Stability of Fully Inorganic Cesium Lead Halide Perovskite Solar Cells, *Nano Lett.*, 2017, **17**(3), 2028–2033.
7 A. Swarnkar, W. J. Mir and A. Nag, Can B-Site Doping or Alloying Improve Thermal- and Phase-Stability of All-Inorganic CsPbX3 (X = Cl, Br, I) Perovskites?, *ACS Energy Lett.*, 2018, **3**(2), 286–289.
8 B. Tang, L. J. Ruan, C. Qin, A. Shu, H. He and Y. Ma, High Stability and Temperature-Dependent Photoluminescence of Orthorhombic CsPbI3 Perovskite Nanoparticles, *Adv. Opt. Mater.*, 2020, **8**(16), 2000498.
9 B. W. Boote, H. P. Andaraarachchi, B. A. Rosales, R. Blome-Fernández, F. Zhu, M. D. Reichert, K. Santra, J. Li, J. W. Petrich and J. Vela, *et al.*, Unveiling the Photo- and Thermal-Stability of Cesium Lead Halide Perovskite Nanocrystals, *Chem. Phys. Chem.*, 2019, **20**(20), 2647–2656.
10 J. S. Han, Q. V. Le, J. Choi, K. Hong, C. W. Moon, T. L. Kim, H. Kim, S. Y. Kim and H. W. Jang, Air-Stable Cesium Lead Iodide Perovskite for Ultra-Low Operating Voltage Resistive Switching, *Adv. Funct. Mater.*, 2018, **28**(5), 1705783.
11 A. Marronnier, G. Roma, S. Boyer-Richard, L. Pedesseau, J.-M. Jancu, Y. Bonnassieux, C. Katan, C. C. Stoumpos,

M. G. Kanatzidis and J. Even, Anharmonicity and Disorder in the Black Phases of Cesium Lead Iodide Used for Stable Inorganic Perovskite Solar Cells, *ACS Nano*, 2018, **12**(4), 3477–3486.

12 G. E. Eperon, G. M. Paternò, R. J. Sutton, A. Zampetti, A. A. Haghighirad, F. Cacialli and H. J. Snaith, Inorganic Caesium Lead Iodide Perovskite Solar Cells, *J. Mater. Chem. A*, 2015, **3**(39), 19688–19695.

13 T. Zhang, M. I. Dar, G. Li, F. Xu, N. Guo, M. Grätzel and Y. Zhao, Bication Lead Iodide 2D Perovskite Component to Stabilize Inorganic A-$CsPbI_3$ perovskite Phase for High-Efficiency Solar Cells, *Sci. Adv.*, 2017, **3**(9), e1700841.

14 W. Xiang, Z. Wang, D. J. Kubicki, W. Tress, J. Luo, D. Prochowicz, S. Akin, L. Emsley, J. Zhou and G. Dietler, *et al.*, Europium-Doped CsPbI2Br for Stable and Highly Efficient Inorganic Perovskite Solar Cells, *Joule*, 2019, **3**(1), 205–214.

15 H. Zhao, J. Xu, S. Zhou, Z. Li, B. Zhang, X. Xia, X. Liu, S. Dai and J. Yao, Preparation of Tortuous 3D γ-$CsPbI_3$ Films at Low Temperature by CaI_2 as Dopant for Highly Efficient Perovskite Solar Cells, *Adv. Funct. Mater.*, 2019, **29**(27), 1808986.

16 A. K. Jena, A. Kulkarni, Y. Sanehira, M. Ikegami and T. Miyasaka, Stabilization of α-$CsPbI_3$ in Ambient Room Temperature Conditions by Incorporating Eu into $CsPbI_3$, *Chem. Mater.*, 2018, **30**(19), 6668–6674.

17 A. Shpatz Dayan, B.-E. Cohen, S. Aharon, C. Tenailleau, M. Wierzbowska and L. Etgar, Enhancing Stability and Photostability of $CsPbI_3$ by Reducing Its Dimensionality, *Chem. Mater.*, 2018, **30**(21), 8017–8024.

18 J.-F. Liao, H.-S. Rao, B.-X. Chen, D.-B. Kuang and C.-Y. Su, Dimension Engineering on Cesium Lead Iodide for Efficient and Stable Perovskite Solar Cells, *J. Mater. Chem. A*, 2017, **5**(5), 2066–2072.

19 Y. Wang, T. Zhang, M. Kan, Y. Li, T. Wang and Y. Zhao, Efficient α-$CsPbI_3$ Photovoltaics with Surface Terminated Organic Cations, *Joule*, 2018, **2**(10), 2065–2075.

20 F. Li, Y. Pei, F. Xiao, T. Zeng, Z. Yang, J. Xu, J. Sun, B. Peng and M. Liu, Tailored Dimensionality to Regulate the Phase Stability of Inorganic Cesium Lead Iodide Perovskites, *Nanoscale*, 2018, **10**(14), 6318–6322.

21 Q. Wang, Z. Jin, D. Chen, D. Bai, H. Bian, J. Sun, G. Zhu, G. Wang and S. F. Liu, M-Graphene Crosslinked $CsPbI_3$ Quantum Dots for High Efficiency Solar Cells with Much Improved Stability, *Adv. Energy Mater.*, 2018, **8**(22), 1800007.

22 H. Bian, D. Bai, Z. Jin, K. Wang, L. Liang, H. Wang, J. Zhang, Q. Wang and S. F. Liu, Graded Bandgap $CsPbI_{2+x}Br_{1-x}$ Perovskite Solar Cells with a Stabilized Efficiency of 14.4%, *Joule*, 2018, **2**(8), 1500–1510.

23 J. W. Lee and N. G. Park, Chemical Approaches for Stabilizing Perovskite Solar Cells, *Advanced Energy Materials*, John Wiley & Sons, Ltd, 2020, 1, p 1903249.

24 B. Zhao, S. F. Jin, S. Huang, N. Liu, J. Y. Ma, D. J. Xue, Q. Han, J. Ding, Q. Q. Ge and Y. Feng, *et al.*, Thermodynamically Stable Orthorhombic γ-$CsPbI_3$ Thin Films for High-Performance Photovoltaics, *J. Am. Chem. Soc.*, 2018, **140**(37), 11716–11725.

25 K. Wang, Z. Jin, L. Liang, H. Bian, D. Bai, H. Wang, J. Zhang, Q. Wang and S. Liu, All-Inorganic Cesium Lead Iodide Perovskite Solar Cells with Stabilized Efficiency beyond 15%, *Nat. Commun.*, 2018, **9**(1), 1–8.

26 P. Zhao, B. J. Kim, X. Ren, D. G. Lee, G. J. Bang, J. B. Jeon, W. B. Kim and H. S. Jung, Antisolvent with an Ultrawide Processing Window for the One-Step Fabrication of Efficient and Large-Area Perovskite Solar Cells, *Adv. Mater.*, 2018, **30**(49), 1802763.

27 M. I. Saidaminov, A. L. Abdelhady, B. Murali, E. Alarousu, V. M. Burlakov, W. Peng, I. Dursun, L. Wang, Y. He and G. MacUlan, *et al.*, High-Quality Bulk Hybrid Perovskite Single Crystals within Minutes by Inverse Temperature Crystallization, *Nat. Commun.*, 2015, **6**, 7586.

28 E. M. Sanehira, A. R. Marshall, J. A. Christians, S. P. Harvey, P. N. Ciesielski, L. M. Wheeler, P. Schulz, L. Y. Lin, M. C. Beard and J. M. Luther, Enhanced Mobility $CsPbI_3$ Quantum Dot Arrays for Record-Efficiency, High-Voltage Photovoltaic Cells, *Sci. Adv.*, 2017, **3**(10), eaao4204.

29 A. Shpatz Dayan, B. E. Cohen, S. Aharon, C. Tenailleau, M. Wierzbowska and L. Etgar, Enhancing Stability and Photostability of $CsPbI_3$ by Reducing Its Dimensionality, *Chem. Mater.*, 2018, **30**(21), 8017–8024.

30 A. Shpatz Dayan, X. Zhong, M. Wierzbowska, C. E. M. de Oliveira, A. Kahn and L. Etgar, The Properties, Photovoltaic Performance and Stability of Visible to near-IR All Inorganic Perovskites, *Mater. Adv.*, 2020, **1**(6), 1920–1929.

31 G. Maculan, A. D. Sheikh, A. L. Abdelhady, M. I. Saidaminov, M. A. Haque, B. Murali, E. Alarousu, O. F. Mohammed, T. Wu and O. M. Bakr, $CH_3NH_3PbCl_3$ Single Crystals: Inverse Temperature Crystallization and Visible-Blind UV-Photodetector, *J. Phys. Chem. Lett.*, 2015, **6**(19), 3781–3786.

32 G. Maculan, A. D. Sheikh, A. L. Abdelhady, M. I. Saidaminov, M. A. Haque, B. Murali, E. Alarousu, O. F. Mohammed, T. Wu and O. M. Bakr, $CH_3NH_3PbCl_3$ Single Crystals: Inverse Temperature Crystallization and Visible-Blind UV-Photodetector, *J. Phys. Chem. Lett.*, 2015, **6**(19), 3781–3786.

33 M. Bender, The Use of Light Scattering for Determining Particle Size and Molecular Weight and Shape, *J. Chem. Educ.*, 1952, **29**(1), 15–23.

34 N. Joong Jeon, J. Hong Noh, Y. Chan Kim, W. Seok Yang, S. Ryu and S. Il Seok, *Solvent Engineering for High-Performance Inorganic–Organic Hybrid Perovskite Solar Cells*. 2014.

35 M. Flatken, A. Hoell, R. Wendt, E. Härk, A. Dallmann, A. Prause, J. Pascual, E. Unger and A. Abate, Small-Angle Scattering to Reveal the Colloidal Nature of Halide Perovskite Precursor Solution, *J. Mater. Chem. A*, 2021, **9**(23), 13477–13482.

36 Q. Zhao, A. Hazarika, L. T. Schelhas, J. Liu, E. A. Gaulding, G. Li, M. Zhang, M. F. Toney, P. C. Sercel and J. M. Luther, Size-Dependent Lattice Structure and Confinement Properties in $CsPbI_3$ Perovskite Nanocrystals: Negative Surface Energy for Stabilization, *ACS Energy Lett.*, 2020, **5**(1), 238–247.

37 Z. Wen, W. Zhai, C. Liu, J. Lin, C. Yu, Y. Huang, J. Zhang and C. Tang, Controllable Synthesis of $CsPbI_3$ Nanorods with Tunable Photoluminescence Emission, *RSC Adv.*, 2019, **9**(43), 24928–24934.

38 D. Vinci, M. Donaldson, J. P. Hallett, E. A. John, P. Pollet, C. A. Thomas, J. D. Grilly, P. G. Jessop, C. L. Liotta and C. A. Eckert, Piperylene Sulfone: A Labile and Recyclable DMSO Substitute, *Chem. Commun.*, 2007, 1427–1429.

39 M. Krumrey and G. Ulm, High-Accuracy Detector Calibration at the PTB Four-Crystal Monochromator Beamline, *Nucl. Instrum. Methods Phys. Res., Sect. A*, 2001, **467**(468), 1175–1178.

40 A. Hoell; I. Zizak; H. Bieder and L. Mokrani German Patent No. DE102006029449 2007.

41 U. Keiderling, The New 'BerSANS-PC'Software for Reduction and Treatment of Small Angle Neutron Scattering Data, *Appl. Phys. A: Mater. Sci. Process.*, 2002, **74**(1), 1455–1457.

42 I. Breßler, J. Kohlbrecher and A. F. Thünemann, SASfit: A Tool for Small-Angle Scattering Data Analysis Using a Library of Analytical Expressions, *J. Appl. Crystallogr.*, 2015, **48**, 1587–1598.

43 A. Vrij, J. W. Jansen, J. K. G. Dhont, C. Pathmamanoharan, M. M. Kops-Werkhoven and H. M. Fijnaut, Light Scattering of Colloidal Dispersions in Non-Polar Solvents at Finite Concentrations: Silica Spheres as Model Particles for Hard-Sphere Interactions, *Faraday Discuss. Chem. Soc.*, 1983, **76**, 19–35.

44 D. Orsi, A. Fluerasu, A. Moussaïd, F. Zontone, L. Cristofolini and A. Madsen, Dynamics in Dense Hard-Sphere Colloidal Suspensions, *Phys. Rev. E: Stat., Nonlinear, Soft Matter Phys.*, 2012, **85**(1), 1–9.

45 D. Frenkel and S. Auer, Prediction of Absolute Crystal-Nucleation Rate in Hard-Sphere Colloids, *Nature*, 2001, **409**(February), 1020–1023.

46 J. K. Percus and G. J. Yevick, Analysis of Classical Statistical Mechanics by Means of Collective Coordinates*, *Phys. Rev.*, 1958, **110**(1), 1–13.

47 A. Vrij, Mixtures of Hard Spheres in the Percus–Yevick Approximation. Light Scattering at Finite Angles, *J. Chem. Phys.*, 1979, **3267**(71), 3267–3270.